MIT Open Access Articles

Pluto's global surface composition through pixel-by-pixel Hapke modeling of New Horizons Ralph/LEISA data

Pluto's global surface composition through pixel-by-pixel Hapke modeling of New Horizons Ralph/LEISA data

S. Protopapa[a], W. M. Grundy[b], D.C. Reuter[c], D.P. Hamilton[a], C. M. Dalle Ore[d,e], J.C. Cook[f], D.P. Cruikshank[e], B. Schmitt[g], S. Philippe[g], E. Quirico[g], R. P. Binzel[h], A.M. Earle[h], K. Ennico[f], C.J.A. Howett[f], A.W. Lunsford[c], C. B. Olkin[f], A. Parker[f], K.N. Singer[f], A. Stern[f], A. J. Verbiscer[j], H. A. Weaver[i], L.A. Young[f], the New Horizons Science Team

[a]*University of Maryland, Department of Astronomy, College Park, Maryland 20742, USA*
[b]*Lowell Observatory, Flagstaff, Arizona 86001, USA*
[c]*National Aeronautics and Space Administration Goddard Space Flight Center, Greenbelt, Maryland 20771, USA*
[d]*SETI Institute*
[e]*NASA Ames Research Center*
[f]*Southwest Research Institute, Boulder, Colorado 80302, USA*
[g]*Institut de Planétologie et Astrophysique de Grenoble, UGA / CNRS, IPAG, Grenoble Cedex 9, France*
[h]*Massachusetts Institute of Technology*
[i]*Johns Hopkins University Applied Physics Laboratory*
[j]*University of Virginia*

Abstract

On July 14th 2015, NASA's New Horizons mission gave us an unprecedented detailed view of the Pluto system. The complex compositional diversity of Pluto's encounter hemisphere was revealed by the Ralph/LEISA infrared spectrometer on board of New Horizons. We present compositional maps of Pluto defining the spatial distribution of the abundance and textural properties of the volatiles methane and nitrogen ices and non-volatiles water ice and tholin. These results are obtained by applying a pixel-by-pixel Hapke

radiative transfer model to the LEISA scans. Our analysis focuses mainly on the large scale latitudinal variations of methane and nitrogen ices and aims at setting observational constraints to volatile transport models. Specifically, we find three latitudinal bands: the first, enriched in methane, extends from the pole to 55°N, the second dominated by nitrogen, continues south to 35°N, and the third, composed again mainly of methane, reaches 20°N. We demonstrate that the distribution of volatiles across these surface units can be explained by differences in insolation over the past few decades. The latitudinal pattern is broken by Sputnik Planitia, a large reservoir of volatiles, with nitrogen playing the most important role. The physical properties of methane and nitrogen in this region are suggestive of the presence of a cold trap or possible volatile stratification. Furthermore our modeling results point to a possible sublimation transport of nitrogen from the northwest edge of Sputnik Planitia toward the south.

1. Introduction

NASA's New Horizons mission completed a close approach to the Pluto system on 14 July 2015 reaching a distance of 12,000 km from the dwarf planet's surface (Stern et al., 2015). A wealth of ground-based data of the Pluto system had been collected prior to the New Horizons mission, motivated first by its status as the outermost planet and later by its being among the few trans-Neptunian objects (TNOs) bright enough for detailed studies to further advance our knowledge of the Kuiper Belt.

The synergy of ground-based observations, modeling efforts and labora-

tory studies have highlighted over the course of the past years, among other things, 1) the presence of methane (CH_4), nitrogen (N_2), carbon monoxide (CO) and ethane (C_2H_6) ices on Pluto together with tholins, 2) constraints on Pluto's surface temperature, and 3) the state of CH_4 ice. CH_4, N_2, and CO ices were detected through ground-based measurements in the near-infrared wavelength range (Cruikshank et al., 1976; Owen et al., 1993). While CH_4 is the most spectroscopically active constituent among Pluto's ices, with several strong absorption bands, CO and N_2 were identified by the detection of the bands at 2.35 μm, as well as the weaker band at 1.58 μm, and 2.15 μm, respectively. Models of Pluto's near-infrared reflectance spectra including C_2H_6 yield an improved reduced χ^2, leading to the conclusion that this ice is also present on the surface of the planet (DeMeo et al., 2010; Holler et al., 2014; Merlin, 2015). The red slope of Pluto's continuum (Bell et al., 1979; Grundy and Fink, 1996; Lorenzi et al., 2016) observed from the visible to around $\sim$1 μm has been attributed to the presence of organic materials on the surface of the body, such as tholins. These are the refractory residues obtained from the irradiation of gases and ices containing hydrocarbons (Cruikshank et al., 2005). In the case of Pluto, tholins may form in situ through energetic processing of CH_4 and N_2 ices (Cruikshank et al., 2016). The spectral profile of the 2.15-μm N_2 absorption band is temperature dependent (Grundy et al., 1993; Tryka et al., 1993) and transitions from broad to very narrow according to whether N_2 is in the hexagonal β- (above 35.6 K) or cubic α-phase, respectively. Tryka et al. (1994), using N_2 as a spectral 'thermometer', inferred a surface temperature of 40$\pm$2 K. At such temperature, thermodynamic equilibrium dictates that pure CH_4 ice cannot co-exist with pure N_2 ice. If both

3

species are present, then instead of pure ices the phases are (Trafton, 2015): CH_4 saturated with N_2 ($\overline{\mathbf{CH_4}}$:N_2) and N_2 saturated with CH_4 ($\overline{\mathbf{N_2}}$:CH_4). The solubility limits of CH_4 and N_2 in each other are temperature dependent and are equal to about 5% ($\overline{\mathbf{N_2}}$:CH_4, with 5% CH_4) and 3% ($\overline{\mathbf{CH_4}}$:N_2 with 3% N_2) at 40 K (Prokhvatilov and Yantsevich, 1983). CH_4 when dissolved in N_2 presents absorption bands shifted toward shorter wavelengths compared to the central wavelengths of pure CH_4 (Quirico and Schmitt, 1997; Grundy et al., 2002). This shift, which is wavelength dependent and is observed in Pluto spectra (Owen et al., 1993), varies with the CH_4 abundance in the mixture: the larger the CH_4 concentration the smaller the blueshift (Schmitt and Quirico, 1992; Quirico and Schmitt, 1997; Protopapa et al., 2015).

While ground-based measurements have played a remarkable role in the growth of knowledge about Pluto's composition (Cruikshank et al., 2015a), they were limited in providing composition maps of Pluto. From the ground, it is possible to investigate changes of Pluto surface composition with longitude by comparing measurements obtained at different rotational phases. Variations with latitude can be determined only by monitoring Pluto as it moves around the Sun during the 248 year orbit. However, over time scales of years, Pluto might undergo a resurfacing process (Stern et al., 1988; Buie et al., 2010a,b). N_2, CO, and CH_4 ices are all volatiles at Pluto surface temperature, of which CH_4 is the least volatile, and support Pluto's atmosphere. Changes in insolation over the course of a Pluto's orbit can result in the bulk migration of volatile ices (Spencer et al., 1997; Hansen and Paige, 1996; Young, 2012, 2013; Hansen et al., 2015). It is therefore difficult to disentangle temporal and spatial variations using ground-based observations

4

(Grundy et al., 2013, 2014).

New Horizons provided a detailed snapshot of the Pluto system with the goal, among others, to map Pluto surface composition and search for additional surface species (Young et al., 2008). New Horizons confirmed the presence on Pluto surface of the volatile ices N_2, CH_4, and CO and detected the existence of the non-volatile water (H_2O) and possibly methanol (CH_3OH) ices (Grundy et al., 2016; Cook et al., 2016). The detection of H_2O-ice did not come as a surprise given that most TNOs are characterized by H_2O-ice dominated spectra (Barucci et al., 2008). Furthermore, Triton, which is thought to be a former TNO captured into a retrograde orbit around Neptune (Agnor and Hamilton, 2006), presents a near-infrared spectrum similar to that of Pluto with clear evidence of H_2O-ice absorption bands (Quirico et al., 1999; Cruikshank et al., 2000). Contrary to Triton (Cruikshank et al., 1993), Pluto does not display the signatures of carbon dioxide (CO_2) ice on the surface (Grundy et al., 2016).

New Horizons revealed striking variations in the distribution of Pluto's ices (Grundy et al., 2016). These results rely on the analysis of spectral parameters, including band depth and equivalent width. However, the main limitation of that approach is the incapability of disentangling relative abundance from grain size effects. This is possible only by means of radiative transfer modeling of the absorption bands over a wide wavelength range, a method that has its own limitations (see Section 5). In this paper, we will discuss constraints on the abundances and scattering properties of the materials across the surface of Pluto, focusing mainly on the distribution of N_2 and CH_4 ices and the relation between their distribution and surface

geology, which is vital to set observational constraints for volatile transport models (Young, 2013; Hansen et al., 2015; Bertrand and Forget, 2016).

2. Observations

Spatially resolved near-infrared spectra of Pluto's surface were acquired using the Linear Etalon Imaging Spectral Array (LEISA), part of the New Horizons Ralph instrument (Reuter et al., 2008). LEISA consists of a wedged filter placed in close proximity to a 256×256 pixels detector array. The filter consists of two segments covering the wavelength range 1.25-2.5 μm and 2.1-2.25 μm at the resolving power ($\lambda/\Delta\lambda$) of 240 and 560, respectively. The low-resolution 1.25-2.5 μm segment is used to infer the surface composition of Pluto as outer solar system ices such as N_2, CH_4, H_2O have strong unique absorption bands in this wavelength region. The high-resolution 2.1-2.25 μm segment is instead sensitive to the spectral shape of the 2.15-μm absorption band of N_2 ice, which is temperature dependent, as well as to the spectral shape and position of the 2.2-μm absorption band of CH_4 ice, which is important to assess the CH_4 to N_2 mixing ratio. The wavelength varies along the row direction of the detector array. LEISA is operated in a scanning mode. A series of image frames, N, are acquired while scanning the field of view across the target surface in a push broom fashion. The target moves through the image plane, along the spectral direction, also called along-track direction. A process of co-registration of each wavelength image is applied, removing motion and optical distortions, to obtain a three-dimensional array spectral cube where each frame images the target surface at a distinct LEISA wavelength. The same process of co-registration is applied to gen-

erate a wavelength spectral cube, such that each pixel has its own spectral array. This way we take into account an existing spectral distortion ('smile') of 2-3 spectral elements along the 256 scanning cross-track pixels due to a slight curvature induced by the filter deposition process.

In this paper we present two LEISA resolved scans of Pluto collected at a distance from Pluto's center of ∼100,000 km at a spatial scale of 6 and 7 km/pixel (see Table 1 for details). The LEISA data presented here have been calibrated through the most up-to-date pipeline processing, which includes bad pixel masking, flat fielding, and conversion from DN to radiance I expressed in erg s^{-1}cm^{-2}Å^{-1}str^{-1}. The latter is normalized by the incoming solar flux to obtain reflectance (I/F). Efforts to improve the radiometric calibration and flat-field are currently underway. Improvements will probably be made as more spectral data from Pluto and Charon are downlinked and become available. The possible impact of calibration changes have been considered in the results presented here.

The last step in the data processing consists of determining the Pluto latitude and longitude corresponding to each LEISA pixel. Integrated Software for Imagers and Spectrometers (ISIS, https://isis.astrogeology.usgs.gov/) provided by the United States Geological Survey (USGS) uses the spacecraft attitude history, which is measured and recorded as part of the standard housekeeping data, along with its LEISA camera model and the reconstructed spacecraft trajectory to determine where each LEISA pixel falls on the target body. We used the ISIS software to perform an orthographic projection of the LEISA data to a sphere at the target's size and location relative to the spacecraft as of the mid-time of each scan. The two LEISA scans

7

presented in this paper combined cover Pluto's full disk and they were both projected to a common orthographic viewing geometry appropriate for the mid-time between the two. The re-projection was done to a target grid with a spatial scale of 2 km/pixel, a higher resolution than the native LEISA pixel scales (see Table 1). The point of sub-sampling is to minimize degradation of spatial information as a result of the nearest neighbor re-sampling. Using the ISIS "translate" routine, we applied a global shift of the LEISA data (consistent across all LEISA wavelengths) to correct for a few pixels mismatch between the LEISA cube and the much higher resolution base map obtained with the Long Range Reconnaissance Imager (LORRI, Cheng et al., 2008) projected to the same geometry. We took into account higher order corrections by means of the ISIS "warp" routine. This is based on a user supplied control network constructed using features that were recognizable in both LEISA and LORRI data. These corrections resulted in LEISA cubes estimated to be geometrically accurate to a little better that a single LEISA pixel. The mid-scan geometry was taken as a reasonable approximation of the illumination and viewing geometry for each pixel.

The modeling analysis presented in this paper is conducted on the LEISA scans degraded to a spatial resolution of ∼12 km/pixel through bin averaging. The mean absolute deviation of the incident and emergent angles within a bin is generally less than ∼0.2 deg but at the limb where it approaches ∼1 deg. The two scans overlap in a region crossing Elliot Crater[1] and Sputnik Planitia. To assess the error in the I/F data introduced by variations in the

---

[1] All place names used in this paper are informal designations

Table 1: Details of the LEISA scans presented in this paper.

Request ID	P_LEISA_Alice_2a	P_LEISA_Alice_2b
MET	299171897	299172767
S/C Start Time, UTC	2015-07-14	2015-07-14
	09:26:19	09:40:49
Phase [deg]	21.7	22.4
SubSol Lat [deg]	51.6	51.6
SubSol Lon [deg]	133.4	132.9
SubS/C Lat [deg]	38.8	38.2
SubS/C Lon [deg]	158.6	158.7
Spatial Scale [km/px]	7	6

quality of the flat-field, scattered light, and other spatially correlated noise sources, we compared the two scans in the region of overlap. A variety of statistical comparisons all consistently produce a conservative estimate of 5% as the mean 1σ uncertainty contributed by these sources of error.

3. Spectral Modeling

The goal of our analysis is to understand the spatial distribution of the abundance and textural properties of each Pluto's surface component. To this end we performed a pixel-by-pixel modeling analysis of the LEISA spectral cubes. This approach requires the application of the same modeling strategy across the entire visible face of Pluto, so that a systematic and comparative study between the composition of the different surface units can be conducted. This is at the expense of possible compositional peculiarities in small surface areas.

We now describe the modeling of a single pixel LEISA spectrum. We use the scattering radiative transfer model of Hapke (1993) to compute the

bidirectional reflectance r of a particulate surface as

$$r(i, e, g) = \frac{w}{4\pi} \frac{\mu_{0e}}{\mu_e + \mu_{0e}} \{[1 + B(g)]P(g) +$$

$$H(\mu_e)H(\mu_{0e}) - 1\} S(i, e, g). \quad (1)$$

The single scattering albedo w is the ratio of the scattering efficiency to the extinction efficiency ($w = 0$ implies that the particles absorb all the radiation) and it can be computed only if the optical constants n and k, the real and imaginary part of the refractive index, respectively, of the surface component, as a function of the wavelength λ, are known. We adopt the equivalent slab model presented by Hapke (1993) to compute w, given the complex refractive index. Notice that w is a function of the particle's effective diameter D, which is a free parameter in our analysis. The terms μ_{0e} and μ_e are related to the cosine of the incidence angle (i) and emission angle (e), respectively, with additional terms to account for the tilt of the surface, due to surface roughness. The latter is also accounted for by the shadowing function $S(i, e, g)$, which involves the mean slope angle $\bar{\theta}$. The backscatter function $B(g)$ is an approximate expression for the opposition effect and it is given by

$$B(g) = \frac{B_0}{1 + (1/h)\tan(g/2)}, \quad (2)$$

where g is the phase angle, h is the compaction parameter and characterizes the width of the nonlinear increase in the reflectance phase curve with decreasing phase angle (the opposition surge), and B_0 is an empirical factor that represents the amplitude of the opposition effect. We adopt for $P(g)$ a single lobe Henyey and Greenstein function

$$P(g) = \frac{1 - \xi^2}{(1 + 2\,\xi\cos\,g + \xi^2)^{3/2}}, \quad (3)$$

10

where ξ is the cosine asymmetry factor. The Ambartsumian–Chandrasekhar H-functions are computed using the approximation proposed by Hapke (2002).

Equation (1) can be used to compute the bidirectional reflectance of a medium composed of closely packed particles of a single component. However, the surface of interest is a mixture of different constituents (Grundy et al., 2016). Even at the pixel level, more than one component can be present. Therefore, in order to calculate synthetic reflectance spectra for comparison with the observational data, it is necessary to compute the reflectance of a mixture of different types of particles. We have considered an areal (also called geographical) mixture, which consists of materials of different composition and/or microphysical properties that are spatially isolated from one another. We adopt this approach as it is the most simple and it provides satisfactory results. In the case of areal mixture, the bidirectional reflectance spectra of the individual components (r_i) are summed with weights equal to the fractional area of each terrain (F_i), as shown below

$$r = \sum_i F_i r_i \quad \text{where } \sum_i F_i = 1. \tag{4}$$

By considering an areal mixture, we are implying that there is no multiple scattering between different components. Given the definition of bidirectional reflectance by Hapke (1993) as the ratio between the radiance at the detector and the irradiance incident on the medium, we have that $I/F = \pi r$. We set the cosine asymmetry parameter $\xi = -0.3$, the compaction parameter $h = 0.5$, the amplitude of the opposition effect $B_0 = 1$, and mean roughness slope $\overline{\theta} = 10°$, following previous studies (Olkin et al., 2007; Buie et al., 2010b).

The free parameters in our model are effective diameter (D_i) and contribution of each surface terrain to the mixture (F_i) . They are iteratively modified by means of a Levenberg-Marquardt χ^2 minimization algorithm until a best-fit to the observations is achieved.

It is possible to determine a spatial map for the abundance and grain size of each surface material by applying the modeling analysis described above pixel-by-pixel. Notice that we consider the other Hapke parameters to be constant across Pluto's surface.

4. Mixture endmembers

The surface components considered in the mixture are H_2O ice, $\overline{\mathbf{N_2}}$:CH_4 ice, $\overline{\mathbf{CH_4}}$:N_2 ice, and Titan tholin. The choice of the surface terrain units relies on the spectral evidence collected over the course of several years, which are outlined in Section 1. For details about the optical constants used for each surface material see Table 2 and the following discussion.

4.1. Tholins

While there is no doubt about the presence of tholins on the surface of Pluto, the specific type of organic material responsible for Pluto's color, ranging from yellow to red (Stern et al., 2015; Grundy et al., 2016), is still unknown. Different types of tholins have been studied but there are only a few for which optical constants are available (for a review on the different kind of tholins the reader is refereed to de Bergh et al., 2008). In particular, the most common are Triton tholin and Titan tholin, which are obtained by irradiating gaseous mixtures of N_2 and CH_4. The difference between the two is in the initial N_2 to CH_4 gaseous mixing ratio (McDonald et al., 1994;

Table 2: Optical constants

Material	Source	Temperature [K]	Filename	Wavelength range [μm]	Notes
Titan Tholin	Khare et al. (1984)			0.02–920.0	
CH$_4$-ice	Grundy et al. (2002)[1]	39	optcte-Vis+NIR+MIR-CH4cr-I-39K	0.7–5.0	
N$_2$-ice	Grundy et al. (1993)[1]	36.5	optcte-NIR-beta-N2-36.5K	2.062–4.762	N$_2$ is in β-phase. We set $n = 1.23$ and $k = 0$, below 2.1 μm.
N$_2$:CH$_4$-ice	Quirico and Schmitt (1997)[1]	36.5	optcte-NIR-CH4-lowC-beta-N2-36.5K	1–5	β-N$_2$:CH$_4$ solid solution with CH$_4$ concentrations lower than 2%. The absorption coefficient of diluted CH$_4$ is normalized to a concentration of 1.
H$_2$O-ice	Grundy and Schmitt (1998)[1]	40		0.96-2.74	

[1]Optical constants are available at http://ghosst.osug.fr/.

Cruikshank et al., 2005; de Bergh et al., 2008). Spectrally, both types of tholins present a red slope in the visible, but Triton tholin contrary to Titan tholin also displays a red slope in the near-IR. Laboratory measurements are currently underway to obtain refractory tholins particularly relevant to Pluto (Pluto's ice tholin) through UV and low-energy electron bombardment of a mixture of Pluto's ices (N$_2$:CH$_4$:CO = 100:1:1, Materese et al., 2015). A preliminary reflectance spectrum of Pluto's ice tholin has been presented by Cruikshank et al. (2015b, 2016), but no optical constants are available at this time. The spectrum shows a red slope between 0.5 and 1 μm, and turns blue in the range between 1 and 2.5 μm. We adopt Titan tholin in the modeling (see Table 2), given the similar spectroscopic behavior with respect to Pluto's ice tholin. The choice of Titan instead of Triton tholin is further
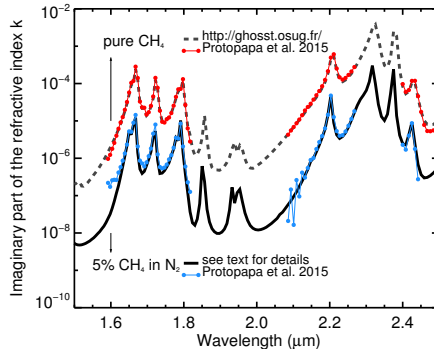
Figure 1: The comparison between the imaginary part of the refractive index, k, of a $\overline{\mathbf{N_2}}$:CH$_4$ mixture with 5% CH$_4$ in N$_2$ computed numerically (black line, see text for details) and measured in the laboratory by Protopapa et al. (2015, blue dots) is shown. For reference, two sets of k for pure CH$_4$ at similar temperatures (gray dashed line and red dots) are shown.

supported by the blue slope of the Pluto/LEISA spectra extracted in the area informally known as Cthulhu Regio, which is a large, dark region along Pluto's equator and one of the darkest and reddest regions on the surface, at visible wavelengths. However, we emphasize that the search for the most appropriate tholin continues and is not the goal of this preliminary study.

4.2. N$_2$-rich and CH$_4$-rich saturated solid solutions

Protopapa et al. (2015) present optical constants for solid solutions of methane diluted in nitrogen (N$_2$:CH$_4$) and nitrogen diluted in methane (CH$_4$:N$_2$) at temperatures between 36 and 90 K, at different mixing ratios http://www2.lowell.edu/users/grundy/abstracts/2015.CH4+N2.html. This set of measurements, which includes optical constants of N$_2$-rich ($\overline{\mathbf{N_2}}$:CH$_4$)

and CH$_4$-rich ($\overline{\mathbf{CH_4}}$:N$_2$) saturated solid solutions, cover the same wavelength range as the LEISA spectrometer. However, they are available in narrow blocks of wavelengths covering regions of intermediate absorption only. This implies that no optical constants are available for $\overline{\mathbf{N_2}}$:CH$_4$ and $\overline{\mathbf{CH_4}}$:N$_2$ around 1.5 and 2.0 μm, where water ice, which turned out to be an undisputed component on the surface of Pluto, presents diagnostic absorption features. While further efforts are being conducted to complete this data set, we adopt optical constants of pure CH$_4$ as a proxy for $\overline{\mathbf{CH_4}}$:N$_2$ and generate optical constants for $\overline{\mathbf{N_2}}$:CH$_4$ following the method described by Douté et al. (1999).

The solubility limit of N$_2$ in CH$_4$ is 3% at 40K. The wavelength shift of the CH$_4$ bands in such a system is smaller than the LEISA resolving power – shifts on the order of $\sim$2$\times$10^{-4} μm are reported by Protopapa et al. (2015), which is over an order of magnitude smaller than the LEISA resolution. Therefore, we do not expect our analysis to be significantly affected by the use of pure CH$_4$ in place of $\overline{\mathbf{CH_4}}$:N$_2$. This is still valid at temperatures lower than 40 K, as the solubility limit of N$_2$ in CH$_4$ decreases with decreasing temperatures (see the CH$_4$-N$_2$ binary phase diagram by Prokhvatilov and Yantsevich, 1983) and smaller shifts correspond to higher CH$_4$ abundances. We use the optical constants of crystalline CH$_4$-I at 39 K from http://ghosst.osug.fr/ (see Table 2 for details). We follow the method described by Douté et al. (1999) to numerically generate optical constants for $\overline{\mathbf{N_2}}$:CH$_4$. We consider two reference components: the first one is identified with pure N$_2$ ice, and the second is CH$_4$ initially diluted in the nitrogen matrix, but artificially normalized to unit concentration (Quirico et al., 1999). Douté et al. (1999)

assume that, for each wavelength, the scalar product of the complex indices of N_2 and the diluted CH_4 by the vector $\left[1\text{-}F^{CH_4}_{\mathbf{N_2:CH_4}}, \; F^{CH_4}_{\mathbf{N_2:CH_4}} \right]$ gives the optical constants of a mixture with a percentage of CH_4 in solid N_2 equal to $F^{CH_4}_{\mathbf{N_2:CH_4}}$. We validate this numerical approach against the optical constants measured by Protopapa et al. (2015) for $F^{CH_4}_{\mathbf{N_2:CH_4}}$=5%, which is the solubility limit of CH_4 in N_2 at 40 K. We use the optical constants for pure N_2 and N_2:CH_4 listed in Table 2. As shown in Figure 1, the numerical approach (black line) well reproduces not only the strengths of the measured (blue dots) CH_4 bands but also that of N_2 at 2.15 μm. The concentration of CH_4 in N_2 ($F^{CH_4}_{\mathbf{N_2:CH_4}}$) is a free parameter in our study.

4.3. H_2O-ice

Laboratory measurements show that infrared water ice absorption bands at 1.5, 1.65 and 2.0 μm change position and shape as a function of phase (crystalline or amorphous) and temperature (Grundy and Schmitt, 1998). We do not solve in this analysis for H_2O-ice temperature and phase and use instead optical constants of crystalline hexagonal water ice at 40 K (see Table 2, http://www2.lowell.edu/users/grundy/abstracts/1998.H2Oice.html).

5. Model discussion

Applying the pixel-by-pixel modeling analysis described in Section 3 is highly computationally expensive. To overcome such limitation, we have implemented our code with multi-threading capabilities. The main code splits the modeling of different surface units across Pluto between multiple

threads of execution. We run our simulations on a multi-processor machine where these threads can execute concurrently. Furthermore, to speed up the task, the pixel-by-pixel modeling analysis is applied to the LEISA data degraded to a spatial resolution of $\sim$12 km/pixel (for a total of $\sim 4 \times 10^4$ pixels to model). Using 15 threads, the modeling of each LEISA scan requires approximately 10 hours.

We present results obtained by applying the Hapke radiative transfer model, assuming an areal mixture of the single endmembers. Several scattering theories (*e.g.*, Shkuratov et al., 1999; Douté and Schmitt, 1998) as well as different types of mixtures (*e.g.,* intimate) exist. These alternative methods could possibly provide similar quality of fits to the data as those presented here but with different percentages and grain size of the components (Poulet et al., 2002). However, we decided to interpret the Pluto New Horizons data with a simple model since it provides a reasonable fit to all 10^4 Pluto spectra (see Section 6). The one presented here is an automated process and a perfect match between observations and the model is beyond the scope of the analysis. Ultimately, the goal is to perform a comparative study between Pluto's main surface units, which can only be done when the same modeling strategy is applied successfully to the full surface of Pluto.

As noted by Barucci et al. (2008), grain size and abundance are sometimes entangled. This occurs mainly when the absolute I/F is unknown and when the analysis is not conducted over a wide wavelength range, which fortunately is not the case for the New Horizons data. We acknowledge that this problem could still arise in absence of defined absorption bands, as in some areas dominated by non-volatile components.

The estimates of the concentration and particle size of each surface compound rely on the choice of the Hapke parameters ξ, h, B_0, and $\overline{\theta}$, since these surface photometric properties affect the entire reflectance spectrum. As discussed in Section 3, we treat these properties as global quantities, constant across all of Pluto's terrains. Given the high degree of surface variations on Pluto, this approximation may not be correct. Work is ongoing to determine the values of these parameters across Pluto's main surface units by inverting the New Horizons Multi-spectral Visible Imaging Camera (MVIC; Reuter et al., 2008) data acquired at different phase angles (Buie et al., 2016). Our analysis will be revisited when the problem of Pluto's photometric properties will be unraveled, which may take some time given its complexity.

While New Horizons confirmed the detection of CO ice on Pluto's surface, mainly in Sputnik Planitia (Grundy et al., 2016), we did not include this component in our models. The main reason is the lack of optical constants in the continuum region, outside of the CO ice absorption bands. Assumptions on the absorption coefficient of CO ice in the continuum region would affect the determination of the abundance and grain size of the other surface compounds, for which optical constants are instead known. We will investigate the inclusion of CO ice in our models as well as other minor species like C_2H_6 in future work.

6. Results

We discuss below the spatial distribution of the abundance and grain size of non-volatiles and volatiles.

6.1. Non-Volatiles

Locations enriched in Titan tholin and H_2O ice are correlated with specific geologic regions (see panels B and D of Figure 2, *e.g.*, Cthulhu Regio, Baré Montes, Piri Planitia, Inanna Fossa, Moore et al., 2016). A change in H_2O-ice abundance and grain size (panels B and C of Figure 2) is observed across these different terrains. In Figure 2 areas of interest are labelled and their corresponding spectra (blue points, with 1σ error estimates), compared with the best fit modeling (red line), are displayed in Figure 3. The spectra are arranged in decreasing H_2O-ice abundance from top to bottom.

The region in the vicinity of Pulfrich crater (region "a") stands out for being particularly enriched in H_2O ice, with abundances close to 60% (see Table 3). The enrichment of H_2O ice in the vicinity of Pulfrich crater is in good agreement with the map displaying the correlation coefficient between each LEISA spectrum and a template Charon-like H_2O ice spectrum (Grundy et al., 2016; Cook et al., 2016). The spectrum extracted in this region (panel "a", Figure 3) shows indeed strong diagnostic absorption bands due to H_2O ice at 1.5 and 2.0 μm, including the 1.65-μm feature, which is characteristic of the crystalline phase of the H_2O ice (Grundy and Schmitt, 1998). The relative strength and shape of the H_2O-ice absorption bands are consistent with grain sizes on the order of $\sim$150 μm. Notice that the best fit modeling suggests the presence not only of H_2O ice but also of tholin and CH_4. The latter produces the absorption bands beyond 2.2 μm. Differences between observations and modeling around 1.4 and 1.7 μm are attributed to flat-fielding, which still requires further optimization. We conclude that across Pluto's encounter hemisphere, no regions of 100% H_2O ice are ob-

served, at this spatial resolution.

The spectrum extracted along Virgil Fossae (region "b") displays a spectral behavior, including the absolute value of I/F, similar to that of Pulfrich crater but with shallower H_2O-ice absorptions. The comparison of the modeling parameters obtained for these two terrains highlights the importance of radiative transfer modeling of the absorption bands to disentangle the effects of grain size, abundance and illumination geometry (see Table 3). The qualitative comparison between these two spectra ("a" and "b") would lead to the conclusion that the fractional abundance of H_2O ice is higher in Pulfrich crater than in Virgil Fossa. While this is still the case, a difference in the particle diameter of H_2O ice is also observed. This is required to take into account the variation in illumination geometry, which plays as important a role as composition and texture in determining the observed spectral properties of the surface.

The spectrum extracted in the Cthulhu Regio (region "c") presents, with respect to the two spectra discussed above, shallower H_2O-ice absorption bands and a neutral spectral slope. This is consistent with smaller H_2O-ice particle diameters ($\sim$10 μm). Furthermore, the absolute value of I/F is lower (on the order of 0.4 instead of 0.6), consistent with a higher abundance of tholins. The spectral effect of tholins is indeed to darken the albedo level, without introducing any significant spectral features. Notice that the absolute I/F values of Titan tholin decrease with increasing grain size. This explains our modeling results, which show regions across Pluto with lower reflectance values (*e.g.*, Cthulhu Regio) corresponding to higher abundances of tholin and larger particle diameters (panels D and E in Figure 2).

20

A few areas across Hayabusa Terra (*e.g.*, region "d") exhibit evidence of H_2O ice. The strong CH_4 absorption features not only beyond 2.2 μm but also across the full wavelength range are indicative of a greater contribution of this ice compared to the previously described regions. At the same time, the presence of H_2O ice is highlighted by the depression in the spectral region around 2.0 μm. These features would not be evident in a spectrum mainly dominated by methane ice, as in the case displayed in panel "e" of Figure 3. It is important to point out that spectra from near the north pole and from most of Tombaugh Regio do not show any spectral evidence for the presence of H_2O ice. On the other hand, the modeling results indicate abundances on the order of 10% and corresponding grain sizes larger than 1000 μm. Synthetic spectra of H_2O ice with such large particles present saturated bands and very low reflectance values. Therefore we infer that water ice in this case is a filling material, spuriously adopted by the modeling code. This is supported by the fact that the model of region "e" with null H_2O ice abundance, provides an equally good fit (comparable χ^2) to the one presented in Figure 2. The absence of H_2O ice mainly affects the grain size and abundance of the tholins, which in this instance have larger values than those reported in Table 3 for case "e". Analogously, the contribution of $\overline{N_2}$:CH_4 in all cases where its abundance is lower than 10% is considered not significant.

6.2. Volatiles

No major region across Pluto's surface is completely depleted of CH_4 (panel A, Figure 4). N_2 on the other hand presents a more localized distribution (panel A, Figure 5). We identify in the volatile maps large scale latitudinal regions, which differ in abundance and texture of the CH_4-rich and N_2-rich

21

components.

The first of these terrains is Lowell Regio, labelled "f" (Figure 4-5). The second is the belt stretching from latitude 35°N to 55°N and crossing Burney Crater and Hayabusa Terra (identified with "g" in Figure 4 and 5). This belt appears to be interrupted by Sputnik Planitia, a deep reservoir of convecting ices (McKinnon et al., 2016a,b; Trowbridge et al., 2016). The relative amount of the CH_4-to-N_2-rich components decreases with decreasing latitude. This is demonstrated by the spectra extracted from representative locations in these two surface units (Figure 6). Spectrum "f", contrary to its counterpart "g", does not display a N_2-absorption feature at $\sim$2.15 μm (vertical dashed line). The modeling indicates a N_2 distribution on the order of 30% and 45% across Lowell Regio and between 35°N and 55°N, respectively (see Table 3). Notice that the presence of an N_2-rich component is marked not only by the $\sim$2.15 μm absorption band but also by the absolute level of the continuum, being higher where N_2 occurs. Furthermore a difference in the path length

Table 3: Models

Region	geometry		H$_2$O		Titan tholin		$\overline{\mathbf{CH_4}}$:N$_2$		$\overline{\mathbf{N_2}}$:CH$_4$		$F_{\overline{\mathbf{N_2}:\mathbf{CH_4}}}^{\mathrm{CH_4}}$	χ^2
	$i[deg]$	$e[deg]$	F[%]	D[μm]	F[%]	D[μm]	F[%]	D[μm]	F[%]	D[μm]	[%]	
a	64	49	60	147	19	37	21	82	0	n/a	n/a	0.78
b	39	35	37	71	48	142	15	376	0	n/a	n/a	1.44
c	55	58	31	11	58	268	11	73	0	n/a	n/a	0.76
d	62	48	26	172	9	38	57	794	8	181252	3.04	1.07
e	34	38	9	3058	12	68	60	695	19	55998	1.61	1.76
f	41	56	8	1270	12	165	53	682	27	62002	5.00	1.86
g	45	67	14	1708	26	424	15	247	45	131197	0.41	2.61
h	36	46	21	46	32	446	43	1137	4	10^7	0.10	2.34
i	57	35	10	2344	9	12	37	1022	43	590952	0.35	1.35
j	31	10	6	1907	18	52	52	941	23	200581	0.53	2.01

of the N_2-rich component is observed, being larger at lower latitudes. This is justified by the N_2 feature getting deeper with larger grains.

Using the MVIC CH_4 equivalent-width map, Grundy et al. (2016) identified another region of interest at low-latitudes at the border of Cthulhu Regio and to the east of Tombaugh Regio, embracing Tartarus Dorsae. This area was identified by a strong 0.89-μm absorption band, possibly due to a higher CH_4 abundance and/or to especially large particle sizes. Our study points out the same area of interest (panel B, Figure 4, region "h") and attributes its peculiarity to particularly large particle sizes ($\sim$1000 μm, see Table 3). While in MVIC observations the diagnostic is the equivalent width of the 0.89-μm CH_4 band, LEISA observations stand out for the broadness of the 2.3-μm CH_4 band (panel "h", Figure 6).

Existing literature on modeling of ground-based near-infrared spectroscopic measurements of Pluto highlights the presence of two "pure" CH_4 components with different grain sizes. The first one is characterized by large mm grains, while the other is described by smaller grains on the order of $\sim$100 μm. This result is obtained when modeling Pluto spectra with intimate (Merlin, 2015) as well as areal mixtures (Protopapa et al., 2008). However, when modeling LEISA spectral data, this distribution of grain sizes is not necessary at the pixel level. We attribute this behavior to the high spatial resolution of the New Horizons data. In fact, the grain size map of the CH_4-rich component presented in this paper shows the presence of regions with particles spanning a range from $\sim$70 μm, to $\sim$1000 μm, justifying the models of the ground-based measurements of Pluto.

The latitudinal pattern described so far is interrupted by Sputnik Plani-

tia, a region set apart by strong 2.15-μm absorption diagnostic of substantial N$_2$ contribution (region "i" in Figure 5). This conclusion was reached already by Grundy et al. (2016) from the analysis of the equivalent width of the 2.15-μm band. However, this is only a rough approximation for the N$_2$ ice abundance. In fact this absorption band is a minor feature on the wings of the 2.2-μm CH$_4$ band and it is only through modeling that its contribution can be isolated and quantified. Three free parameters in our modeling all point to the greater role that N$_2$ plays in this part of Pluto than anywhere else on the encounter hemisphere. They are the large abundance of $\overline{\mathbf{N_2}}$:CH$_4$ (panel A, Figure 5), the small amount of CH$_4$ diluted in N$_2$ (panel C, Figure 5), and the large path length (or equivalently particle diameter D, panel B, Figure 5). Compositional differences are observable within Sputnik Planitia (regions "i" and "j" in Figure 5): the northwest part of Sputnik Planitia presents, with respect to the center, a shallower N$_2$ absorption band, and therefore a smaller abundance of $\overline{\mathbf{N_2}}$:CH$_4$ with higher concentrations of CH$_4$ in N$_2$, and smaller path length (Table 3). This dichotomy is suggestive of a possible transport of N$_2$ from the northwest to the south of Sputnik Planitia (see arrow in Figure 5, panel B). It is likely due to sublimation and redeposition driven by the north-south insolation gradient. Sublimation of N$_2$ in the northwest part of Sputnik Planitia leaves behind CH$_4$, which is less volatile. This would justify the larger amount of CH$_4$ in the N$_2$-rich component, as well as the shrinkage of grains. The larger abundance of $\overline{\mathbf{N_2}}$:CH$_4$ at the center of the basin is instead consistent with condensation of N$_2$.

7. Discussion

We present a quantitative analysis of the spatially resolved spectral maps of Pluto's surface obtained with the New Horizons Ralph/LEISA instrument. This analysis provides constraints on the amount and grain size of Pluto's surface components. The resulting spatial distribution of ices and tholin appears to be mostly consistent with the qualitative analysis performed on the same data set by Schmitt et al. (2016) using different techniques.

Simplifying the compositional findings into rough latitudinal regions, the maps that we have presented in Figs. 2, 4 and 5 give the following broad picture. Straddling Pluto's equator, Cthulhu Regio is a band of low reflectance tholin-like material with very little CH_4 or N_2 signatures. To the north at about $20°$ latitude this transitions to a region of CH_4 rich material, which in turns yields to an N_2 and CH_4 mixture at about $35°$ latitude. Further to the north, by about $55°$ latitude, the N_2 signature smoothly tapers off to an expansive polar plain of predominantly CH_4 ices.

Pluto's intriguing diversity of surface features traces back to its size, which given cold temperatures in the outer Solar System, is sufficient to retain a thin atmosphere. Seasonal deposits and more substantial reservoirs of CH_4 and N_2 ices cover the surface which, in the absence of volatiles, would be expected to be composed principally of water ice (Schaller and Brown, 2007). Our compositional bands are composed of volatile materials and roughly follow lines of latitude, which suggest that insolation is likely controlling the distribution. Conversely, the fact that the boundaries are somewhat ragged and not perfectly aligned with latitude indicates that other effects, likely including surface composition and topography, are important too. We

25

neglect these local effects here, instead concentrating on the global structure apparent in our maps.

The transitions that we find with our maps of volatile cover correlate well with expectations of vigorous spring sublimation after a long polar winter. The Sun returned to illuminate Pluto's north pole in late 1987 and for the past 20 years has been depositing more energy at polar latitudes than in the temperate zone. Continuous illumination northward of $75°$ over the past twenty years, and northward of $55°$ over the past ten years (Figure 7, sunlit fraction equals one), seems to have sublimated the most volatile N_2 into the atmosphere, with the best chance for redeposition occurring at points southward. This loss of surface N_2 appears to have created the polar bald spot seen most clearly in Figure 5 (panel A), shown schematically in Figure 7, and also predicted by Hansen and Paige (1996). This sublimation front is advancing southward ever more rapidly as illumination in the northern hemisphere strengthens.

Regions southward of $35°$ have been exposed to strong solar illumination with average fluxes greater than 0.4 W/m^2 for $\sim$40 years, twice as long as the polar regions (compare with Figure 7). From 1975-1995, these low latitude regions (blue band in Figure 7) experienced much stronger heating than regions to the north, leading to sublimation of N_2 and redeposition of N_2 ice to points northward. We argue that a slowly moving N_2 sublimation front has likely expanded northward from Cthulhu Regio and is destined to meet the more rapidly southward moving polar sublimation front within the decade.

The N_2-rich component dominates mainly in Sputnik Planitia. The ices

26

in this reservoir are the result of long term processes (Spencer et al., 1997; Earle et al., 2015, 2016; Hamilton et al., 2016; Bertrand and Forget, 2016), unlike the seasonal latitudinal bands discussed above. For a plausible Pluto surface temperature of 40 K, the N_2-CH_4 binary phase diagram shows that, in the case of thermodynamic equilibrium and if both the CH_4-rich and N_2-rich components are present, the solubility limit of CH_4 in N_2 is about 5%. However, setting this as a constraint failed to reproduce the strong 2.15-μm N_2 band. If we let the concentration of CH_4 in N_2 vary, we find that amounts close to 0.3% are needed to reproduce the 2.15-μm N_2 band. It is not the first time that such low concentrations of CH_4 in N_2 are adopted in modeling analysis to reproduce Pluto's spectrum (*e.g.*, Douté et al. (1999) obtained 0.36% of CH_4 diluted in N_2 in their best fit model considering geographical mixture). Because we have a finite CH_4-rich component, this finding could be interpreted as a sign of a much lower temperature in Sputnik Planitia, in agreement with that reported by Hamilton (2015). However, a value of 0.36% of CH_4 diluted in N_2 would imply N_2 to be in α-phase, contrary to the evidence collected so far. Because of the uncertainties in the binary phase diagram and because the contribution of CO ice was not taken into account, we leave the temperature interpretation to a further effort which will include the analysis of the 2.1-2.25 μm LEISA segment. Furthermore we intend to explore different modeling approaches, including layering. In fact, the temperature interpretation stands only if the CH_4-rich component is locally present with the N_2-rich one. However, a dynamical differentiation between N_2-rich and CH_4-rich components could occur during sublimation producing possible layering (Stansberry et al., 1996). The physical properties

27

of N_2 across Sputnik Planitia could in fact suggest a possible sublimation transport of this volatile from the northwest to the center.

8. Acknowledgments

References

References

Agnor, C. B., Hamilton, D. P., 2006. Neptune's capture of its moon Triton in a binary-planet gravitational encounter. Nature 441, 192–194.

Barucci, M. A., Brown, M. E., Emery, J. P., Merlin, F., 2008. Composition and Surface Properties of Transneptunian Objects and Centaurs. In: Barucci, M. A., Boehnhardt, H., Cruikshank, D. P., Morbidelli, A., Dotson, R. (Eds.), The Solar System Beyond Neptune. pp. 143–160.

Bell, J. F., Clark, R. N., McCord, T. B., Cruikshank, D. P., 1979. Reflection Spectra of Pluto and Three Distant Satellites. In: Bulletin of the American Astronomical Society. Vol. 11 of Bulletin of the American Astronomical Society. p. 570. Abstract.

Bertrand, T., Forget, F., 2016. Observed glacier and volatile distribution on Pluto from atmosphere-topography processes. Nature, accepted.

Buie, M. W., Grundy, W. M., Young, E. F., Young, L. A., Stern, S. A., 2010a. Pluto and Charon with the Hubble Space Telescope. I. Monitoring Global Change and Improved Surface Properties from Light Curves. The Astronomical Journal 139, 1117–1127.

Buie, M. W., Grundy, W. M., Young, E. F., Young, L. A., Stern, S. A., 2010b. Pluto and Charon with the Hubble Space Telescope. II. Resolving Changes on Pluto's Surface and a Map for Charon. The Astronomical Journal 139, 1128–1143.

Buie, M. W., et al., 2016. Photometric Properties of Pluto. In: Lunar and Planetary Science Conference. Vol. 47 of Lunar and Planetary Science Conference. p. 2927.

Cheng, A. F., et al., 2008. Long-Range Reconnaissance Imager on New Horizons. Space Science Reviews 140, 189–215.

Cook, J. C., et al., 2016. The Identification and Distribution of Pluto's Non-Volatile Inventory. In: Lunar and Planetary Science Conference. Vol. 47 of Lunar and Planetary Science Conference. p. 2296.

Cruikshank, D. P., et al., 2016. Pluto and Charon: The Non-Ice Surface Component. In: Lunar and Planetary Science Conference. Vol. 47 of Lunar and Planetary Science Conference. p. 1700.

Cruikshank, D. P., et al., 2015a. The surface compositions of Pluto and Charon. Icarus 246, 82–92.

Cruikshank, D. P., et al., 2015b. Pluto: Distribution of ices and coloring agents from New Horizons LEISA observations. In: AAS/Division for Planetary Sciences Meeting Abstracts. Vol. 47 of AAS/Division for Planetary Sciences Meeting Abstracts. p. 101.02.

Cruikshank, D. P., Imanaka, H., Dalle Ore, C. M., 2005. Tholins as coloring agents on outer Solar System bodies. Advances in Space Research 36, 178–183.

Cruikshank, D. P., Pilcher, C. B., Morrison, D., 1976. Pluto - Evidence for methane frost. Science 194, 835–837.

Cruikshank, D. P., et al., 1993. Ices on the surface of Triton. Science 261, 742–745.

Cruikshank, D. P., et al., 2000. Water Ice on Triton. Icarus 147, 309–316.

de Bergh, C., Schmitt, B., Moroz, L. V., Quirico, E., Cruikshank, D. P., 2008. Laboratory Data on Ices, Refractory Carbonaceous Materials, and Minerals Relevant to Transneptunian Objects and Centaurs. In: Barucci, M. A., Boehnhardt, H., Cruikshank, D. P., Morbidelli, A., Dotson, R. (Eds.), The Solar System Beyond Neptune. The University of Arizona Press, Tucson, pp. 483–506.

DeMeo, F. E., et al., 2010. A search for ethane on Pluto and Triton. Icarus 208, 412–424.

Douté, S., Schmitt, B., 1998. A multilayer bidirectional reflectance model for the analysis of planetary surface hyperspectral images at visible and near-infrared wavelengths. Journal of Geophysical Research 103, 31367–31390.

Douté, S., et al., 1999. Evidence for Methane Segregation at the Surface of Pluto. Icarus 142, 421–444.

Earle, A. M., et al., 2016. Long-Term Surface Temperature Modeling of Pluto. Icarus, accepted.

Earle, A. M., et al., 2015. Correlating Pluto's Albedo Distribution to Long Term Insolation Patterns. In: AAS/Division for Planetary Sciences Meeting Abstracts. Vol. 47 of AAS/Division for Planetary Sciences Meeting Abstracts. p. 200.05.

Grundy, W. M., et al., 2016. Surface Compositions Across Pluto and Charon. Science 351, aad9189–1.

Grundy, W. M., Fink, U., 1996. Synoptic CCD Spectrophotometry of Pluto Over the Past 15 Years. Icarus 124, 329–343.

Grundy, W. M., Olkin, C. B., Young, L. A., Buie, M. W., Young, E. F., 2013. Near-infrared spectral monitoring of Pluto's ices: Spatial distribution and secular evolution. Icarus 223, 710–721.

Grundy, W. M., Olkin, C. B., Young, L. A., Holler, B. J., 2014. Near-infrared spectral monitoring of Pluto's ices II: Recent decline of CO and N_2 ice absorptions. Icarus 235, 220–224.

Grundy, W. M., Schmitt, B., 1998. The temperature-dependent near-infrared absorption spectrum of hexagonal H_2O ice. Journal of Geophysical Research 103, 25809–25822.

Grundy, W. M., Schmitt, B., Quirico, E., 1993. The Temperature-Dependent Spectra of α and β Nitrogen Ice with Application to Triton. Icarus 105, 254–258.

Grundy, W. M., Schmitt, B., Quirico, E., 2002. The Temperature-Dependent Spectrum of Methane Ice I between 0.7 and 5 μm and Opportunities for Near-Infrared Remote Thermometry. Icarus 155, 486–496.

Hamilton, D., et al., 2016. The icy heart of Pluto. Nature, accepted.

Hamilton, D. P., 2015. The Icy Cold Heart of Pluto. In: AAS/Division for Planetary Sciences Meeting Abstracts. Vol. 47 of AAS/Division for Planetary Sciences Meeting Abstracts. p. 200.07.

Hansen, C. J., Paige, D. A., 1996. Seasonal Nitrogen Cycles on Pluto. Icarus 120, 247–265.

Hansen, C. J., Paige, D. A., Young, L. A., 2015. Pluto's climate modeled with new observational constraints. Icarus 246, 183–191.

Hapke, B., 1993. Theory of reflectance and emittance spectroscopy. In: Topics in Remote Sensing, Cambridge, UK: Cambridge University Press, —c1993.

32

Hapke, B., 2002. Bidirectional Reflectance Spectroscopy. 5. The Coherent Backscatter Opposition Effect and Anisotropic Scattering. Icarus 157, 523–534.

Holler, B. J., Young, L. A., Grundy, W. M., Olkin, C. B., Cook, J. C., 2014. Evidence for longitudinal variability of ethane ice on the surface of Pluto. Icarus 243, 104–110.

Khare, B. N., Sagan, C., Arakawa, E. T., Suits, F., Callcott, T. A., Williams, M. W., 1984. Optical constants of organic tholins produced in a simulated Titanian atmosphere - From soft X-ray to microwave frequencies. Icarus 60, 127–137.

Lorenzi, V., et al., 2016. The spectrum of Pluto, 0.40-0.93 μm. I. Secular and longitudinal distribution of ices and complex organics. Astronomy & Astrophysics 585, A131.

Materese, C. K., Cruikshank, D. P., Sandford, S. A., Imanaka, H., Nuevo, M., 2015. Ice Chemistry on Outer Solar System Bodies: Electron Radiolysis of N2-, CH4-, and CO-Containing Ices. The Astrophysical Journal 812, 150.

McDonald, G. D., Thompson, W. R., Heinrich, M., Khare, B. N., Sagan, C., 1994. Chemical investigation of Titan and Triton tholins. Icarus 108, 137–145.

McKinnon, W. B., et al., 2016a. Thermal Convection in Solid Nitrogen, and the Depth and Surface Age of Cellular Terrain Within Sputnik Planum, Pluto. In: Lunar and Planetary Science Conference. Vol. 47 of Lunar and Planetary Science Conference. p. 2921.

McKinnon, W. B., et al., 2016b. Convection in a volatile nitrogen-ice-rich layer drives Pluto's geological vigour. Nature 534, 82–85.

Merlin, F., 2015. New constraints on the surface of Pluto. Astronomy & Astrophysics 582, A39.

Moore, J. M., et al., 2016. The geology of Pluto and Charon through the eyes of New Horizons. Science 351, 1284–1293.

Olkin, C. B., et al., 2007. Pluto's Spectrum from 1.0 to 4.2 μm: Implications for Surface Properties. The Astronomical Journal 133, 420–431.

Owen, T. C., et al., 1993. Surface ices and the atmospheric composition of Pluto. Science 261, 745–748.

Poulet, F., Cuzzi, J. N., Cruikshank, D. P., Roush, T., Dalle Ore, C. M., 2002. Comparison between the Shkuratov and Hapke Scattering Theories for Solid Planetary Surfaces: Application to the Surface Composition of Two Centaurs. Icarus 160, 313–324.

Prokhvatilov, A. I., Yantsevich, L. D., 1983. X-ray investigation of the equilibrium phase diagram of CH_4-N_2 solid mixtures. Sov. J. Low Temp. Phys., vol. 9, p. 94-98 (1983). 9, 94–98.

Protopapa, S., et al., 2008. Surface characterization of Pluto and Charon by L and M band spectra. Astronomy & Astrophysics 490, 365–375.

Protopapa, S., Grundy, W. M., Tegler, S. C., Bergonio, J. M., 2015. Absorption coefficients of the methane-nitrogen binary ice system: Implications for Pluto. Icarus 253, 179–188.

Quirico, E., et al., 1999. Composition, Physical State, and Distribution of Ices at the Surface of Triton. Icarus 139, 159–178.

Quirico, E., Schmitt, B., 1997. Near-Infrared Spectroscopy of Simple Hydrocarbons and Carbon Oxides Diluted in Solid N $_2$and as Pure Ices: Implications for Triton and Pluto. Icarus 127, 354–378.

Reuter, D. C., et al., 2008. Ralph: A Visible/Infrared Imager for the New Horizons Pluto/Kuiper Belt Mission. Space Science Reviews 140, 129–154.

Schaller, E. L., Brown, M. E., 2007. Volatile Loss and Retention on Kuiper Belt Objects. The Astrophysical Journal 659, L61–L64.

Schmitt, B., et al., 2016. Mixing and Physical State of Pluto's Surface Materials from New Horizons LEISA Spectro-Images. In: Lunar and Planetary Science Conference. Vol. 47 of Lunar and Planetary Science Conference. p. 2794.

Schmitt, B., Quirico, E., 1992. Laboratory Data on Near-Infrared Spectra of Ices of Planetary Interest. In: AAS/Division for Planetary Sciences Meeting Abstracts #24. Vol. 24 of Bulletin of the American Astronomical Society. p. 968.

Shkuratov, Y., Starukhina, L., Hoffmann, H., Arnold, G., 1999. A Model of Spectral Albedo of Particulate Surfaces: Implications for Optical Properties of the Moon. Icarus 137, 235–246.

Spencer, J. R., Stansberry, J. A., Trafton, L. M., Young, E. F., Binzel, R. P., Croft, S. K., 1997. Volatile Transport, Seasonal Cycles, and Atmospheric

Dynamics on Pluto. In: Stern, S. A., Tholen, D. J. (Eds.), Pluto and Charon. p. 435.

Stansberry, J. A., Spencer, J. R., Schmitt, B., Benchkoura, A.-I., Yelle, R. V., Lunine, J. I., 1996. A model for the overabundance of methane in the atmospheres of Pluto and Triton. Planetary and Space Science 44, 1051–1063.

Stern, S. A., et al., 2015. The Pluto system: Initial results from its exploration by New Horizons. Science 350, aad1815.

Stern, S. A., Trafton, L. M., Gladstone, G. R., 1988. Why is Pluto bright? Implications of the albedo and lightcurve behavior of Pluto. Icarus 75, 485–498.

Trafton, L. M., 2015. On the state of methane and nitrogen ice on Pluto and Triton: Implications of the binary phase diagram. Icarus 246, 197–205.

Trowbridge, A. J., Melosh, H. J., Steckloff, J. K., Freed, A. M., 2016. Vigorous convection as the explanation for Pluto's polygonal terrain. Nature 534, 79–81.

Tryka, K. A., Brown, R. H., Anicich, V., Cruikshank, D. P., Owen, T. C., 1993. Spectroscopic determination of the phase composition and temperature of nitrogen ice on Triton. Science 261, 751–754.

Tryka, K. A., Brown, R. H., Cruikshank, D. P., Owen, T. C., Geballe, T. R., de Bergh, C., 1994. Temperature of nitrogen ice on Pluto and its implications for flux measurements. Icarus 112, 513–527.

Young, L. A., 2012. Volatile transport on inhomogeneous surfaces: I - Analytic expressions, with application to Pluto's day. Icarus 221, 80–88.

Young, L. A., 2013. Pluto's Seasons: New Predictions for New Horizons. The Astrophysical Journal Letters 766, L22.

Young, L. A., et al., 2008. New Horizons: Anticipated Scientific Investigations at the Pluto System. Space Science Reviews 140, 93–127.

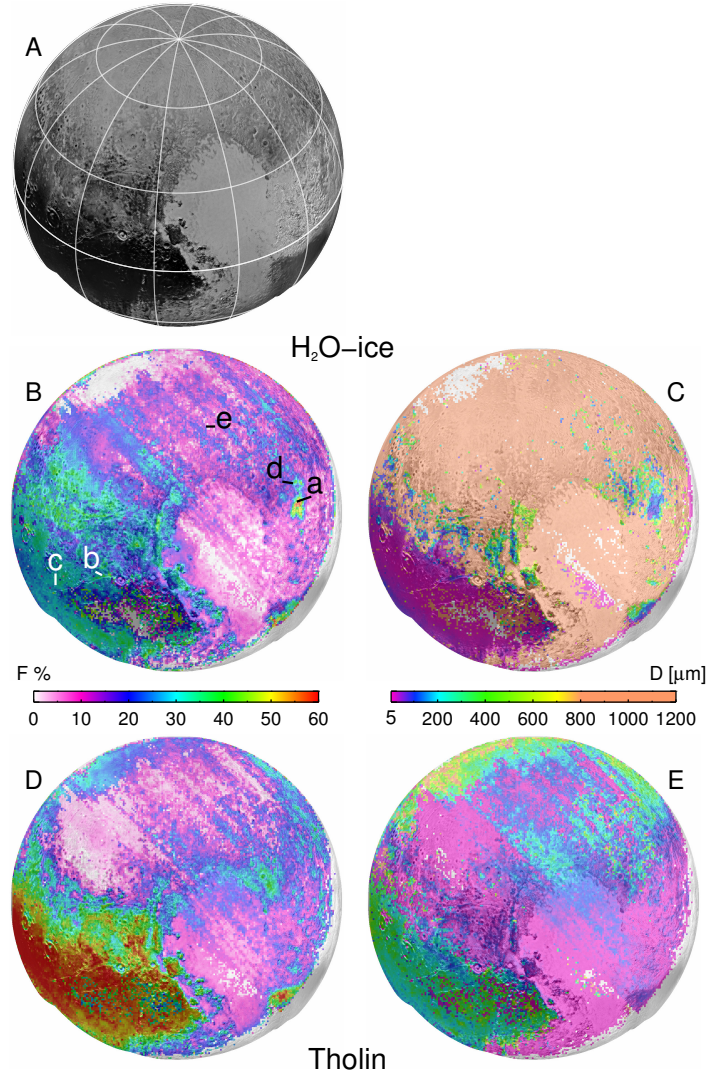Figure 2: Panel A shows the LORRI base map reprojected to the geometry of the LEISA observation. Panels B and C show the pixel-by-pixel modeling results for H$_2$O-ice abundance, F%, and effective diameter, D[μm], superposed on the LORRI base map. Areas of interest discussed in the text are labelled in panel B. Panels D and E show similar maps for Titan tholin. Regions with abundance lower than 10% (white and purple) are below the noise level and therefore should not be overinterpreted.
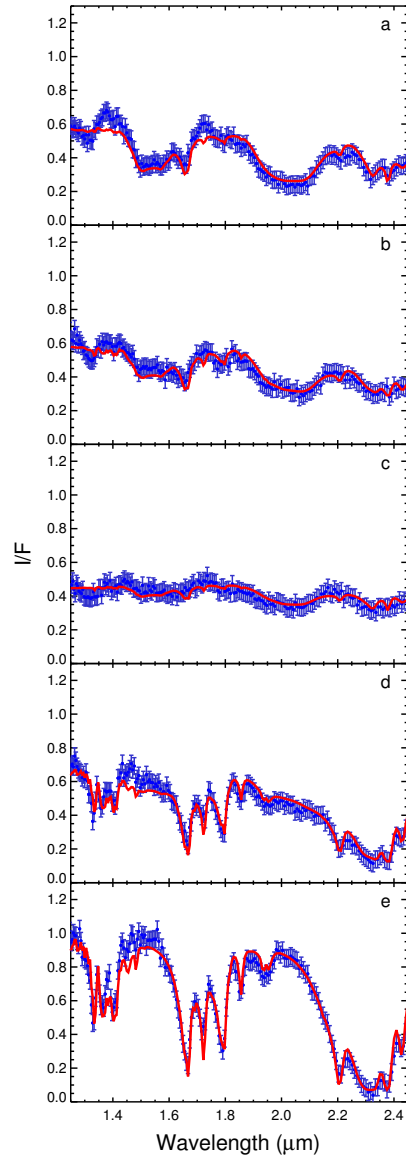
Figure 3: Spectra extracted in regions labelled in Figure 2 are shown as blue dots with 1σ error estimates, and compared with their corresponding best fit models (solid red line).
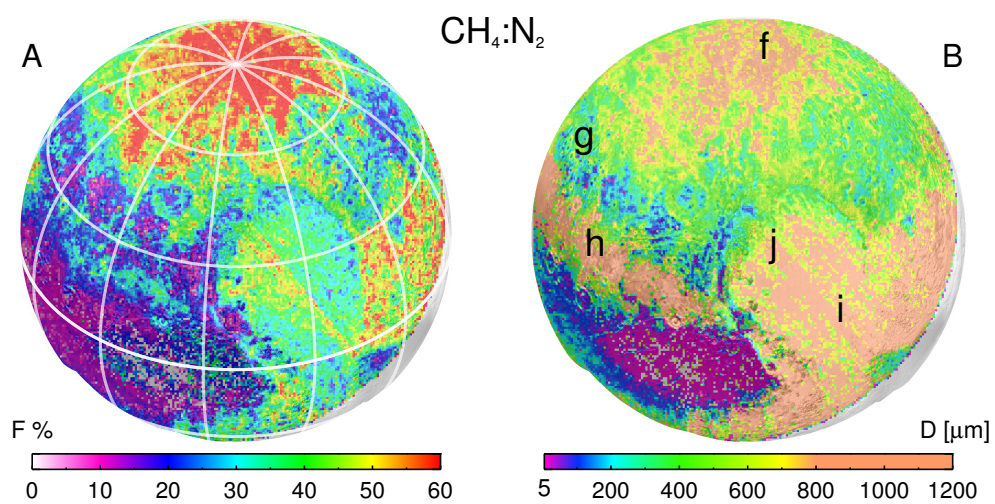
Figure 4: Panels A and B show abundance and effective diameter of the CH$_4$-enriched component, respectively, as obtained from the pixel-by-pixel modeling analysis. The composition maps are superposed on the reprojected LORRI base map. Areas of interest discussed in the text are labelled in panel B.
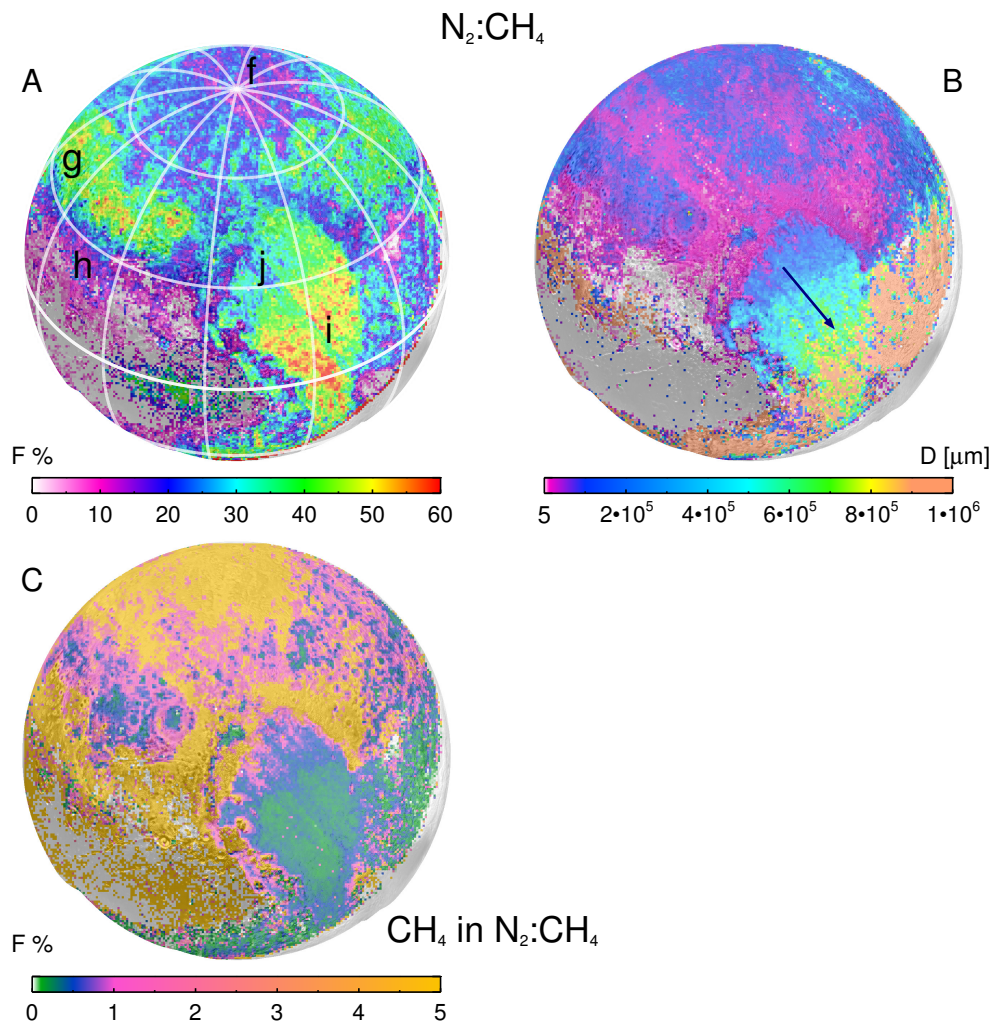
Figure 5: Modeling results relative to abundance and path length of the N_2-enriched component are shown in panels A and B, respectively. Panel C shows the dilution content of CH_4 in N_2. The composition maps are superposed on the reprojected LORRI base map. Areas of interest discussed in the text are labelled in panel A. The arrow in panel B indicates the direction of the N_2 sublimation transport discussed in the text.
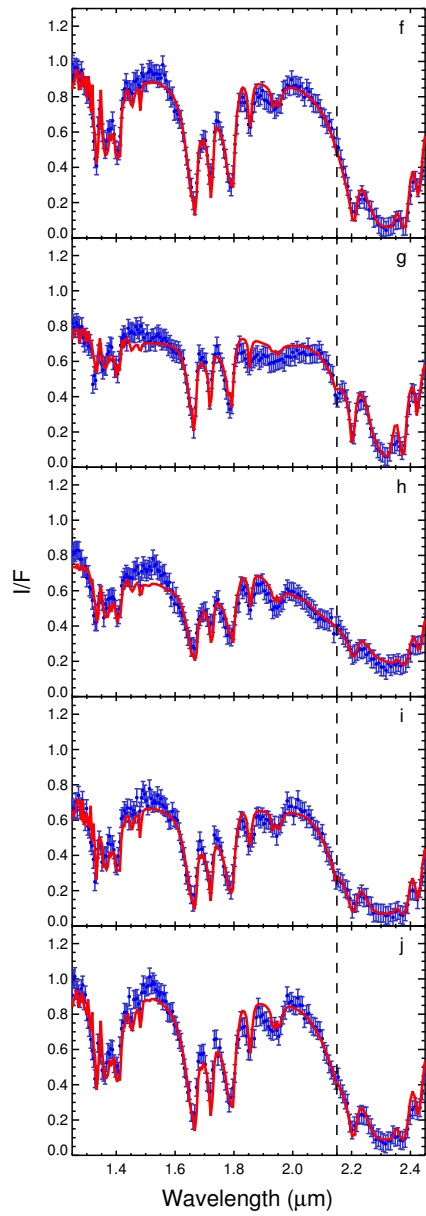
Figure 6: Spectra extracted in regions labelled in Figures 4 and 5 are shown as blue dots and compared with their corresponding best fit modeling (solid red line).
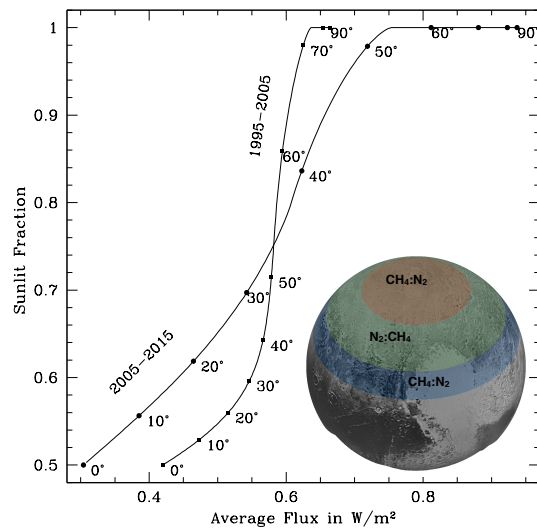
Figure 7: The fraction of a Pluto rotation period that a point at a given latitude is sunlit versus average flux in W/m². Northern latitudes are marked with symbols spaced at 10° intervals. The filled squares show the average energy flux to Pluto's northern hemisphere over the decade 1995-2005 while the filled circles show the same for the past ten years. Pluto's north pole has been sunlit since 1987 and, over the past 20 years, has received more solar illumination than any other latitude. Differences are relatively minor around the turn of the century, but become much more pronounced after 2005. The intense heating correlates well with polar depletion of N_2 (see the reddish circle on the Pluto inset).